



# New gas-filled mode of the large-acceptance spectrometer VAMOS

C. Schmitt, M. Rejmund, A. Navin, B. Lecornu, B. Jacquot, G. de France,  
A. Lemasson, A. Shrivastava<sup>1</sup>

*GANIL, CEA/DSM - CNRS/IN2P3, Bd Henri Becquerel, BP 55027, F-14076 Caen Cedex 5, France*

P. Greenlees, J. Uusitalo

*Department of Physics, University of Jyväskylä, P.O. Box 35, FI-40014, Jyväskylä, Finland*

K. Subotic

*VINCA Institute of Nuclear Sciences, P.O. Box 522, 11001 Belgrade, Serbia*

L. Gaudefroy

*CEA, DAM, DIF, F-91297 Arpajon, France*

Ch. Theisen, B. Sulignano

*CEA-Saclay DSM/IRFU/SPhN, F-91191 Gif/Yvette Cedex, France*

O. Dorvaux, L. Stuttgé

*IPHC, UMR7178, IN2P3-CNRS et Université Louis Pasteur, BP28, F-67037 Strasbourg, France*

---

## Abstract

A new gas-filled operation mode of the large-acceptance spectrometer VAMOS at GANIL is reported. A beam rejection factor greater than  $10^{10}$  is obtained for the  $^{40}\text{Ca}+^{150}\text{Sm}$  system at 196 MeV. The unprecedented transmission efficiency for the evaporation residues produced in this reaction is estimated to be around 80% for  $\alpha xn$  channels and above 95% for  $xnp$  channels. A detailed study of the performance of the gas-filled VAMOS and future developments are discussed. This new operation mode opens avenues to explore the potential of fusion reactions in various kinematics.

*Key words:* Gas-filled spectrometer, Fusion reactions, Beam rejection, Transmission.

---

## 1. Introduction

Fusion-evaporation reactions permit probing the structure and dynamics of fully equilibrated nuclei under extreme conditions of

angular momentum and/or temperature. For discriminating weakly populated evaporation channels from the overwhelming background due to other events, a highly selective and efficient device for detecting the evaporation residues (ERs) around  $0^\circ$  is necessary. This is especially true at high beam intensities, where a good rejection of the unreacted projectile

<sup>1</sup> Permanent Address: Nuclear Physics Division, Bhabha Atomic Research Centre, Mumbai 400085, India

is crucial. Additionally, since the evaporation residues after passing through the target are characterized by broad distributions in angle, energy and charge state, a large angular aperture and a high transport efficiency between the target and the detectors are required.

Depending on the ions involved, different arrangements of optical elements are used to achieve an adequate rejection of the beam and a reasonable collection efficiency of the ERs. While Wien Filters [1] or separated electric and magnetic dipoles [2] are based on a selection in velocity of the incoming ions, recoil mass spectrometers [3] disperse the particles according to their mass over charge state ratio  $M/Q$ . Magnetic spectrometers select the ions depending on the momentum over charge state ratio, or equivalently, magnetic rigidity,  $B\rho = p/Q$ . Gas-filled magnetic separators (Ref. [4] and references therein) take advantage of the difference in the mean charge state  $Q$  reached by beam and ERs along their transport in a gas at low pressure [5], yielding a magnetic rigidity which, to first order, is proportional to the mass of the ion [6]. This, in general, leads to a better rejection of the direct beam as compared to what is achieved in vacuum. Additionally, the  $Q$  distribution is narrow [7], resulting in an enhanced transmission of the ERs. Due to the deterioration of the mass resolution, caused mainly by charge exchange and multiple scattering in the gas, it is customary at gas-filled magnets to isotopically identify the reaction products by their characteristic decay (e.g. [8,9]). Although high beam rejection is currently possible, the transmission is limited by the small acceptance of the existing devices [2,10–13].

Recently, a few large-acceptance magnetic spectrometers [14–17] were built and operated under vacuum. We presently focus on the VARIable MOde Spectrometer (VAMOS) [16,17] at GANIL. VAMOS was originally designed to cope with the challenge inherent to the low-intensity SPIRAL1 radioactive ion beams. High efficiency and isotopic identification of the recoiling ion were among the major goals. Different modes of operation are available depending on the settings of the optical elements. The versatility of VAMOS has been exploited for the study of various mechanisms such as deep-inelastic collisions [18],

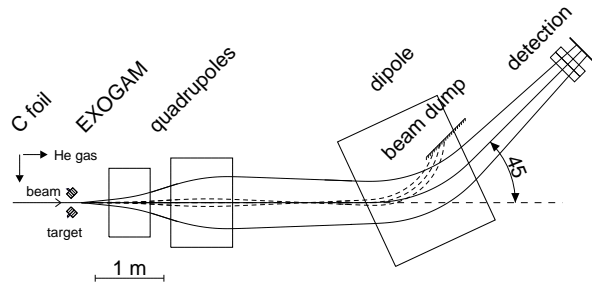


Fig. 1. Schematic layout of the spectrometer and detection system. VAMOS was placed at  $0^\circ$  with respect to the beam axis. The focal plane detection system consists of two drift chambers followed by a Si wall and a Plastic scintillator. Typical trajectories calculated with ZGOUBI [22] for different angles at the target for beam particles (dashed lines) and evaporation residues (full lines) are shown.

fission [19] and direct reactions [20]. Isotopic identification of the reaction products was achieved up to  $A \sim 160$ . The present communication reports on the recent implementation of a gas-filled operation mode at VAMOS. This upgrade considerably extends the capabilities of the device when operated at  $0^\circ$ . To characterize the new operation mode of VAMOS, a fusion reaction studied previously [8] at gas-filled separators was used. Ion-optical calculations were performed to quantify the transmission of the ERs. The limitations of the new operation mode were identified, and further improvements are discussed.

## 2. Measurement and experimental results

### 2.1. Experimental set-up

The measurement was made using a  $^{40}\text{Ca}$  beam at 196 MeV, delivered by the CSS1 cyclotron of GANIL, incident on a  $550 \mu\text{g}/\text{cm}^2$  thick  $^{150}\text{SmF}_3$  target evaporated on a carbon backing ( $25 \mu\text{g}/\text{cm}^2$ ). A schematic of the experimental set-up is shown in Fig. 1. The spectrometer consisted of a quadrupole doublet and a magnetic dipole (QQD configuration). The Wien filter was not used in the present work. The optical axis of VAMOS was placed at  $0^\circ$  with respect to the beam axis. The first quadrupole was placed at 40 cm from the target, and the dipole bending angle was  $45^\circ$ . Both the distance to the target and the dipole bending angle are variable at VAMOS [17]. In

the present configuration, a large acceptance in angle ( $\Omega \sim 60$  msr) and in magnetic rigidity ( $\Delta B\rho/B\rho \approx \pm 7\%$ ) is achieved, and the maximum magnetic rigidity  $B\rho_{max}$  is 1.8 T-m. A carbon foil  $\sim 100 \mu\text{g}/\text{cm}^2$  thick was placed 1 m upstream of the target to isolate the beam line from the gas-filled region. The whole section ( $\sim 8.6$  m) between the carbon foil and the end of the detection chamber was filled with He gas at low pressure ( $p$  was varied between 0.1 and 1.4 mbar). The nominal magnetic rigidity  $B\rho_0$ , which defines the central (reference) trajectory, was varied around the  $B\rho$  value predicted by model calculations for the ERs produced in the reaction. The deflected direct beam was stopped inside the dipole chamber in a "rake-like" plate made of tantalum and small aluminium pieces for minimizing the particles scattered onto the focal plane. The detection system consisted of two position-sensitive drift chambers (DCs), a windowless  $500 \mu\text{m}$  thick Si wall (2 rows with 9 detectors of  $5 \text{ cm} \times 7 \text{ cm}$  size each) and a 15 mm thick Plastic scintillator. The prompt  $\gamma$ -rays emitted by the reaction products at the target were detected using four segmented EXOGAM Ge clover detectors [21] placed at backward angles. For each event, the position ( $x_1, x_2, y_1, y_2$ ) on the drift chambers, the energy loss  $\Delta E = \Delta E_1 + \Delta E_2$  in the DCs, the residual energy  $E_{Si}$  in the Si wall, the charge  $Q_{Pl}$  induced in the Plastic scintillator, and the time-of-flight between the target and the focal plane were recorded. The time-of-flight was derived using the timing signal of the Si detectors with respect to either the time of the  $\gamma$ -ray detectors ( $T_{of}$ ) or the frequency of the cyclotron ( $T_{Si-hf}$ ).

The magnetic rigidity  $B\rho$ , angles ( $\theta, \phi$ ) at the target position and path along the spectrometer were software reconstructed on an event-by-event basis [17] from the measured positions on the DCs. When combined with the time-of-flight, the trajectory reconstruction permits the determination of the velocity vector of the recoiling nucleus at the target position. The angle between the crystal of the EXOGAM clover detector and the reconstructed velocity was used to obtain the Doppler correction to be applied to the  $\gamma$ -ray spectrum [17]. The energy loss  $\Delta E$ , residual energy  $E_{Si}$  and charge  $Q_{Pl}$  were used for tagging the reaction. The ERs produced in the collision were iso-

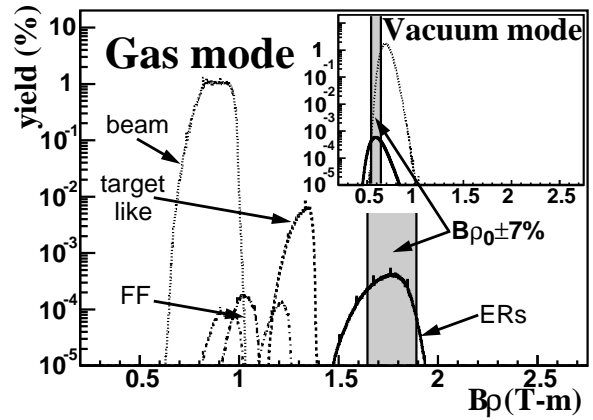


Fig. 2. Calculated magnetic rigidity distribution for the products of the  $^{40}\text{Ca}+^{150}\text{Sm}$  collision at 196 MeV. The  $B\rho$  distribution at the focal plane of the gas-filled VAMOS as obtained with ANAMARI [26] assuming  $p = 0.6$  mbar is shown for the direct beam (dotted line) and the most probable reaction channels: target-like nuclei (dashed line), typical fission-fragment products (dashed-dotted lines) and ERs (full line). The inset shows the  $B\rho$  distribution for direct beam (dotted line) and ERs (full line) as calculated for the vacuum mode. The shaded areas define the acceptance of the spectrometer for ERs.

topically identified by the measurement of the characteristic prompt  $\gamma$ -rays emitted at the target and/or the radioactive  $\alpha$ -decay in the Si detectors.

The time-of-flight and energy loss were calibrated using SRIM08 calculations [23] for the ERs produced in the reaction. The Si detectors were gain matched with a pulse generator and calibrated using a  $^{233}\text{U}$ - $^{239}\text{Pu}$ - $^{241}\text{Am}$   $\alpha$ -source. The resolution was typically  $\sim 60$  keV (FWHM). The energy of the heavy ions implanted in the Si detectors computed with the  $\alpha$ -calibration was corrected for pulse height defect following the procedure given in Ref. [24]. The four EXOGAM clovers were calibrated using standard sources, and the total photopeak efficiency was  $\sim 3.5\%$  at 1 MeV.

The fusion cross section for the present reaction was estimated to be  $\sim 240$  mb using a statistical model code [25]. The excited  $^{190}\text{Pb}$  compound nucleus decays either by fission (75%) or particle evaporation (25%). The  $B\rho$  distribution at the focal plane of the gas-filled VAMOS calculated by the ANAMARI code [26] is shown in Fig. 2 for the unreacted projectiles and the dominant reaction channels. The calculation takes into account the charge equilibration, angular scattering and energy straggling in the

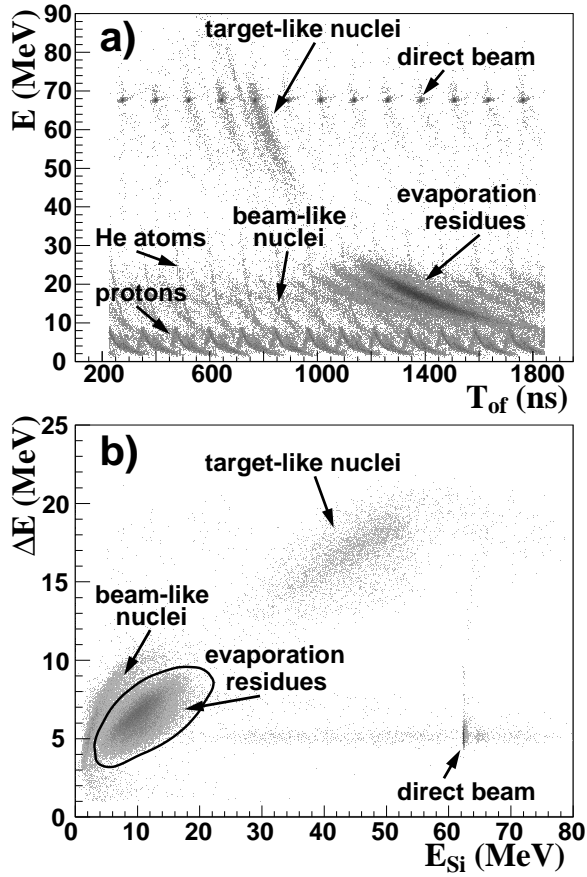


Fig. 3. Particle identification for  $B\rho_0 = 1.5$  T-m and  $p = 0.1$  mbar. a) Correlation between the total energy  $E = \Delta E + E_{Si}$  and the time-of-flight  $T_{of}$ . Repetition of the structures every 122 ns is due to the cycling of the beam. b) Correlation between the energy loss  $\Delta E$  and the residual energy  $E_{Si}$ . The contour illustrates the gate applied for selecting ERs. In both panels, the contributions from the various kinds of particles are indicated. Note the saturation of the signal for direct beam particles in the Si detectors.

target and gas. The acceptance of the spectrometer for ERs is indicated by the shaded area. The ERs are predicted to be well separated from the direct beam and other reaction products and efficiently transmitted ( $\sim 85\%$  of them reach the detectors for  $p = 0.6$  mbar). The inset shows the  $B\rho$  distribution calculated for the beam and ERs with the spectrometer in the vacuum mode, demonstrating the gain in beam rejection and transmission achieved by the gas-filled mode. With the vacuum mode of VAMOS, either the Wien Filter [27] or the dispersive QQD mode achieves sufficient beam rejection in very asymmetric direct kinematics. For more symmetric and inverse kinemat-

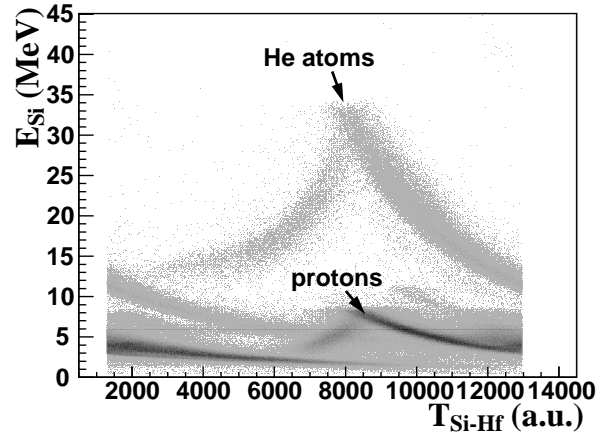


Fig. 4. Light-particle spectrum for  $B\rho_0 = 1.57$  T-m and  $p = 0.12$  mbar. Correlation between the energy  $E_{Si}$  and the time-of-flight  $T_{Si-hf}$  for events in anti-coincidence with the DCs.

ics, the measurements are restricted to low-intensity beams.

## 2.2. Particle identification and characterization of the evaporation residues

The evaporation residues can in principle be discriminated from other reaction products using the correlation between the measured total energy  $E = \Delta E + E_{Si}$  and the time-of-flight  $T_{of}$ . Such a correlation is shown in Fig. 3a. The direct beam and target-like nuclei can be seen to be well separated from the ERs. Beam-like particles scattered from the beam dump, protons originating from reactions in the beam dump as well as scattered He gas atoms can also be observed. These overlap in the  $(E, T_{of})$  region of the evaporation residues, making the clean selection of the ERs based only on total energy and time-of-flight difficult. The measured energy loss was used for a further selection (Fig. 3b). The evaporation residues are well separated from beam-like particles in the  $(\Delta E, E_{Si})$  correlation. The signals induced by proton and He light particles are too low to trigger the DCs. These light particles lead to a non-negligible background in the energy spectrum of the radioactive  $\alpha$ -decay of the ERs. Figure 4 shows the correlation between the energy deposited in the Si detectors  $E_{Si}$  and the time-of-flight  $T_{Si-hf}$ . To select light particles, an anti-coincidence with the DCs was required. Two intense structures are observed, correspond-

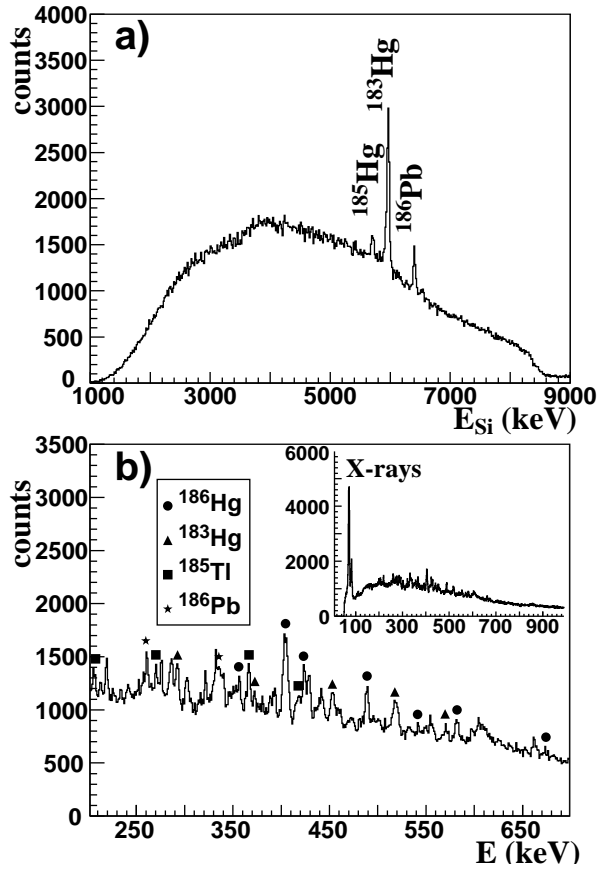


Fig. 5. Isotopic identification of the evaporation residues. a) Spectrum of the  $\alpha$ -decay of the ERs at the focal plane. The peaks are labelled by the parent nucleus. b) Selected region of the Doppler-corrected  $\gamma$ -ray spectrum in prompt coincidence with ERs. The main ERs are labelled. The characteristic X-rays can be seen in the inset.

ing to the protons produced in the beam dump and the scattered gas atoms. The fold-back in these structures at 9 and 32 MeV is consistent with the range of, respectively, protons and He particles in 500  $\mu\text{m}$  of Si. The left (right) branch of each structure corresponds to those particles which punch through (stop in) the Si detectors. The He atoms were found to be absent in the spectrum for a run collected during the measurement with VAMOS under vacuum. Protons were detected even in the absence of a target, and the correlation between their measured energy and time-of-flight was found to be consistent with the distance between the beam dump and the detectors. To reduce the background caused by these light particles in the Si detectors, the Plastic scintillator was used as a veto.

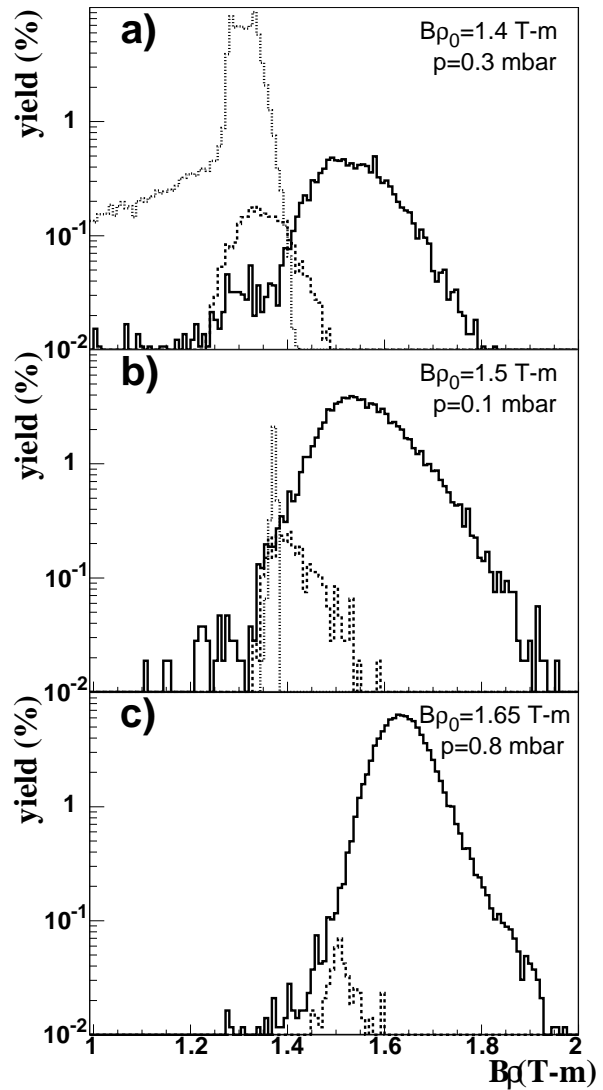


Fig. 6. Experimental magnetic rigidity distribution. Reconstructed  $B\rho$  of direct beam (dotted lines), target-like nuclei (dashed lines) and ERs (full lines) for different experimental conditions: a)  $B\rho_0 = 1.4$  T-m and  $p = 0.3$  mbar, b)  $B\rho_0 = 1.5$  T-m and  $p = 0.1$  mbar, c)  $B\rho_0 = 1.65$  T-m and  $p = 0.8$  mbar.

The spectrum of the residual energy  $E_{Si}$  obtained from the events in anti-coincidence with both the DCs and the Plastic detector is shown in Fig. 5a. The observed peaks are assigned to the radioactive  $\alpha$ -decay of  $^{185}\text{Hg}$  ( $E_\alpha = 5653$  keV),  $^{183}\text{Hg}$  ( $E_\alpha = 5904$  keV) and  $^{186}\text{Pb}$  ( $E_\alpha = 6332$  keV). The large size of the individual Si detectors used in the present work did not permit the correlation of the ER implantation with its decay at the focal plane. The implantation rate

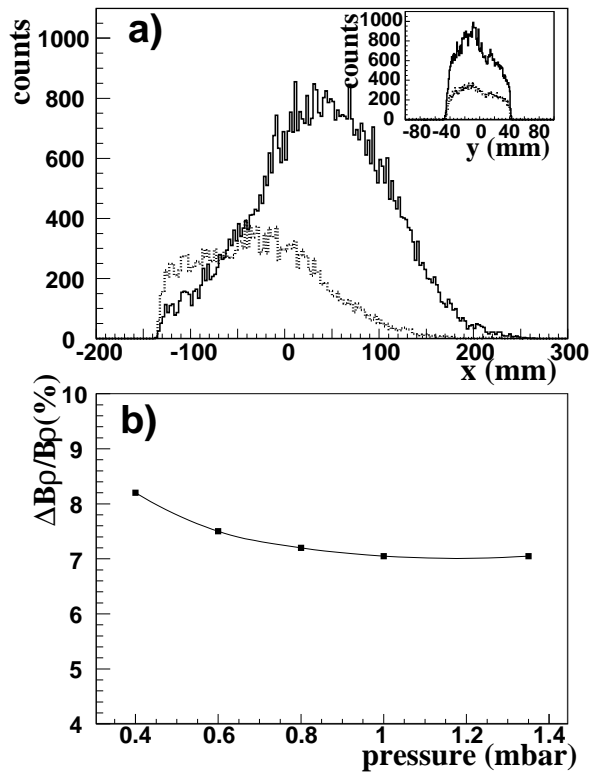


Fig. 7. Distribution of the evaporation residues. a) Distribution of the ERs in the horizontal (dispersive) direction at the focal plane for  $p = 0.8$  mbar and two settings:  $B\rho_0 = 1.57$  T-m (dashed line) and  $B\rho_0 = 1.65$  T-m (full line). The distributions in the vertical direction are shown in the inset. The two settings were normalized to the incident beam intensity. b) Width of the measured  $B\rho$  for ERs as a function of the He gas pressure for  $B\rho_0 = 1.65$  T-m.

in one Si detector was larger than the inverse of the half-life of the ERs. To improve this aspect, an upgrade of the set-up is discussed in section 4.

The Doppler-corrected  $\gamma$ -ray spectrum in prompt coincidence with the ERs is shown in Fig. 5b. The most intense  $\gamma$ -ray transitions observed are from  $^{186}\text{Hg}$  (2p2n),  $^{183}\text{Hg}$  ( $\alpha$ 3n),  $^{185}\text{Tl}$  (p4n) and  $^{186}\text{Pb}$  (4n). Note that the  $^{183}\text{Hg}$  and  $^{186}\text{Pb}$  nuclei appear in both the prompt  $\gamma$ -ray and the  $\alpha$ -decay spectra. The  $^{186}\text{Hg}$  residue decays through  $\beta$ -radioactivity to a stable nuclide, and its production was inferred only from the  $\gamma$ -ray spectrum. The  $^{185}\text{Tl}$  nucleus preferentially decays by  $\beta$ -radioactivity to  $^{185}\text{Hg}$ , the  $\alpha$ -decay of which was measured in the Si detectors.

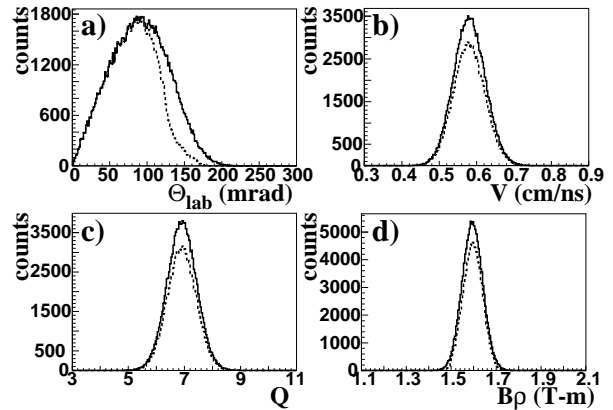


Fig. 8. Simulation for the  $^{183}\text{Hg}$  evaporation residues. The distribution in a) angle in the laboratory frame  $\Theta_{lab}$ , b) velocity  $V$ , c) charge state  $Q$  and d) magnetic rigidity  $B\rho$  are shown. The full lines represent the incident particles, while the dashed lines comprise only those particles which are transmitted.

### 3. Performance of the gas-filled VAMOS

#### 3.1. Beam rejection

Figure 6 shows the measured  $B\rho$  distribution for the direct beam, target-like nuclei and ERs. The various particles have been selected applying a condition on the  $(\Delta E, E_{Si})$  correlation. The distributions are shown for three different values of  $B\rho_0$ . The measurement compares well with the ANAMARI calculation (Fig. 2). With increasing nominal rigidity, the yields of the direct beam and target-like nuclei decrease due to their lower  $B\rho$ . For a value of  $B\rho_0 = 1.65$  T-m, no un-reacted projectile was detected at the focal plane for a beam intensity of  $1.2 \times 10^{10}$  particles/s within a run of  $\sim 30$  min. The rejection factor for the direct beam is therefore estimated to be better than  $10^{10}$ . The current usable during the present measurement was limited by the counting rate in the Ge detectors due to reactions induced in fluorine in the target and in the carbon backing.

#### 3.2. Transmission of the evaporation residues

The spatial distribution of the ERs at the focal plane was studied as a function of both the nominal rigidity and the He gas pressure. The distribution was found to be centred on the detectors and narrowest for  $B\rho_0 = 1.65$  T-m and  $p \sim 1$  mbar (Fig. 7a and b, respectively). These

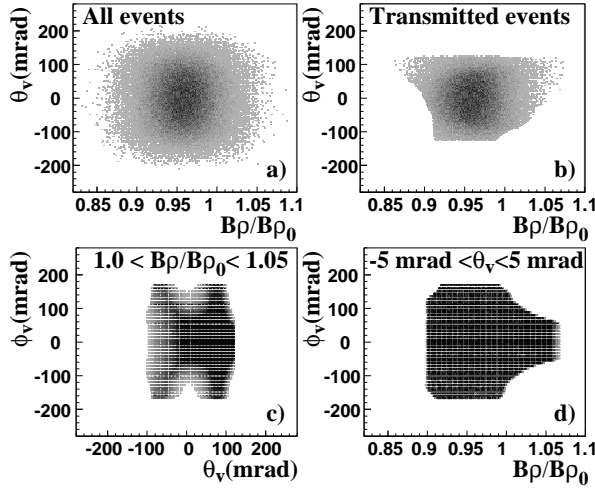


Fig. 9. Acceptance of VAMOS. a) Correlation between the relative magnetic rigidity  $B\rho/B\rho_0$  and the azimuthal angle  $\theta_v$  for the simulated  $^{183}\text{Hg}$  evaporation residues. b) Identical to a) for those ions which reach the detection system. Acceptance map of VAMOS c) in the  $(\theta_v, \phi_v)$  plane for  $1.0 < B\rho/B\rho_0 < 1.05$  and d) in the  $(B\rho/B\rho_0, \phi_v)$  plane for  $-5 \text{ mrad} < \theta_v < +5 \text{ mrad}$ .

values are in agreement with model calculations [26] and previous measurements [5, 13]. The measured minimal width of the  $B\rho$  distribution of  $\sim 6\%$  is comparable to that measured at other gas-filled separators for similar reactions (Ref. [4] and references therein).

The transmission of a given evaporation residue is defined as the ratio of the number of residues reaching the focal plane detectors and the number of residues produced in the target. The transmission depends on the kinematics of the reaction and the acceptance of the spectrometer [12, 17, 28]. Monte-Carlo simulations were performed to understand quantitatively the measurements at the focal plane, and unfold the role of the reaction kinematics and the finite acceptance of the spectrometer. The angle and energy distribution of the ERs after the target was calculated based on fusion-evaporation kinematics [29] for those evaporation residues observed in the measurement. The charge state distribution acquired by the ion along its transport in the gas was modelled following Ref. [5]. Figure 8 shows the simulated distribution as a function of laboratory angle  $\Theta_{lab}$ , velocity  $V$ , charge state  $Q$  and magnetic rigidity  $B\rho$  for the  $\alpha^3\text{n}$  channel ( $^{183}\text{Hg}$ ). The transport of the particle through VAMOS was derived using

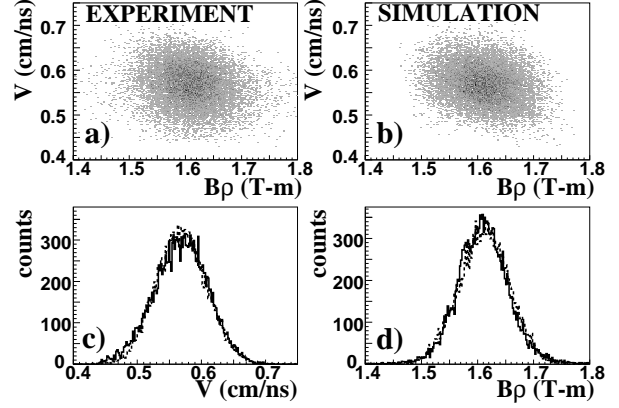


Fig. 10. Comparison of the measurement with the simulation for  $B\rho_0 = 1.65 \text{ T-m}$  and  $p = 0.6 \text{ mbar}$ . Correlation between the velocity  $V$  and the magnetic rigidity  $B\rho$  of the ERs as extracted a) from the experiment and b) from the calculation. The projections on the  $V$  and  $B\rho$  axis are shown in panel c) and d), respectively, for the measurement (full lines) and the calculation (dashed lines).

ion-optical calculations performed with the ZGOUBI code [22] in the three-dimensional  $(B\rho/B\rho_0, \theta_v, \phi_v)$  phase space. The subscript  $v$  refers to the coordinate system of the spectrometer [17]. A point-like beam was assumed. The charge exchange process along the transport in the gas was simulated by the use of a continuous charge state distribution (Fig. 8c). Model calculations [26] show that the dominant contribution to angular scattering of the ERs is due to the target. The above assumptions are sufficient for the present purpose of determining the beam envelope along the optical elements [30]. The influence of the acceptance on the transmission of the  $^{183}\text{Hg}$  evaporation residue is illustrated in the upper panel of Fig. 9, where the relative magnetic rigidity  $B\rho/B\rho_0$  is plotted as a function of the azimuthal angle  $\theta_v$ . The simulated distribution of  $^{183}\text{Hg}$  at the entrance of VAMOS is shown in panel a), while only the transmitted residues are displayed in panel b). The initial distribution is observed to be modified in a non-uniform manner as a result of the complex transport efficiency of the spectrometer in the  $(B\rho/B\rho_0, \theta_v, \phi_v)$  phase space. The calculated acceptance map of VAMOS is shown in the lower panels of Fig. 9 as a function of  $(\theta_v, \phi_v)$  and  $(B\rho/B\rho_0, \phi_v)$  for relevant ranges of  $B\rho/B\rho_0$  and  $\theta_v$ . The loss of transmission observed at  $B\rho/B\rho_0 \geq 1$  for  $\theta_v \sim 0$  in Fig. 9b is found to arise from the limited range in  $\phi_v$  covered by

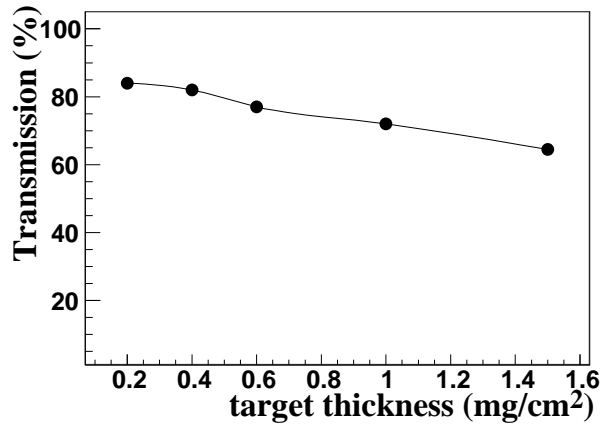


Fig. 11. Transmission as a function of the target thickness. Calculated transmission at VAMOS for the  $^{183}\text{Hg}$  evaporation residue produced in the reaction  $^{40}\text{Ca}+^{150}\text{Sm}$  at 196 MeV.

the spectrometer at large rigidities. The results of the calculation for the transmitted  $^{183}\text{Hg}$  residues are compared with the input distributions in Fig. 8. A detailed study of the transport efficiency at VAMOS can be found in [17]. A similar study was recently reported for the vacuum spectrometer PRISMA [31]. Figure 10 shows the comparison of the  $B\rho$  and  $V$  distributions for the measurement and the calculation (including all ERs). The good agreement between the simulated and the measured values shows that the present method can be used for reliably estimating the transport efficiency. For the  $^{40}\text{Ca}+^{150}\text{Sm}$  reaction at 196 MeV, the transmission was found to be better than 95% for nucleon (n and/or p) evaporation channels and  $\sim 80\%$  for  $\alpha$  evaporation channels. The sensitivity of the calculation was estimated to be less than 10%. The relatively low transmission quoted for the  $\alpha$  channels is limited by the angular spread caused by the evaporated  $\alpha$  particle (Fig. 8a). This is not applicable for xn evaporation channels which are characterized by emission angles smaller than the angular aperture of VAMOS. The evolution of the transmission as a function of the target thickness for the  $\alpha 3n$  evaporation channel is shown in Fig. 11.

The knowledge of the transport efficiency and the number of characteristic  $\alpha$  decays measured at the focal plane were used to estimate partial ER production cross sections. These were found to be in reasonable agreement with previous measurements [32] and

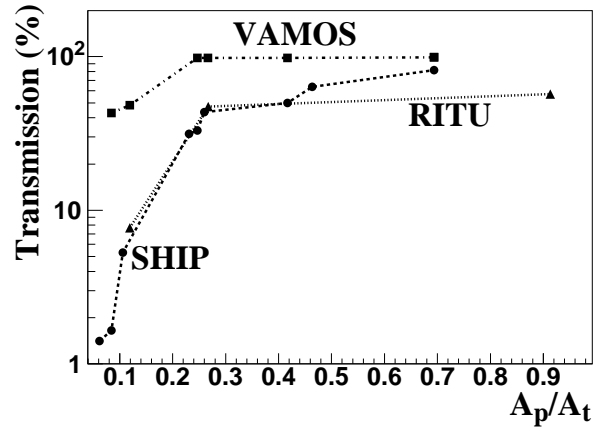


Fig. 12. Comparison of the transmission at VAMOS (squares), SHIP (circles) and RITU (triangles) as a function of the ratio between the projectile and target masses ( $A_p/A_t$ ). The transmissions quoted are for a given ER after neutron evaporation. The values were taken from Ref. [28] and Ref. [13] for SHIP and RITU respectively. The systems considered range from  $^{12}\text{C}$  (60 MeV)+ $^{142}\text{Nd}$  to  $^{84}\text{Kr}$  (336 MeV)+ $^{92}\text{Mo}$ . The lines are to guide the eye.

statistical model calculations [25]. Under the present conditions a cross section of the order of  $\sim 30 \mu\text{b}$  was measurable.

The present work is the first application of trajectory reconstruction methods for a gas-filled magnet. The reconstruction of the magnetic rigidity permits an efficient determination of the optimal settings for the measurement. This is especially crucial when rare processes are to be investigated [33]. Additionally, the reconstructed velocity vector of the residue at the target improves the Doppler correction of the emitted  $\gamma$ -rays. This aspect will be important for an efficient use of next generation  $\gamma$ -arrays [34]. The large path length and  $B\rho$  limitations in VAMOS makes it unsuitable for the study of super heavy nuclei in reactions with lead or actinide targets. With the advent of the next generation radioactive beam facility SPIRAL2 at GANIL, the gas-filled mode of VAMOS would be suitable for symmetric reactions and inverse kinematics.

### 3.3. Comparison with existing separators

The main characteristics of routinely used gas-filled separators are summarized in Table 1. As can be seen from the table, the arrangement of the optical elements at VAMOS differs from the commonly used DQQ config-

Table 1

Characteristics of existing gas-filled separators. For VAMOS the numbers refers to the current configuration.

	SASSYER [35]	DGFRS [36]	GARIS [37]	BGS [38]	RITU [39]	TASCA [30]	VAMOS [17]
Optics	DQD	DQQ	DQQ(D)	QDD	QDQQ	DQQ	QQD
$\Omega$ (msr)	7	10	22	45	10	5-10	60
$B\rho_{max}$ (T-m)	2.2	3.1	1.85	2.5	2.2	3	1.8
Length (m)	4	4.3	4.8	4.7	4.7	4	7.6
Bending angle (deg)	23	23	45	70	25	23	45
Dispersion (cm/%)	0.67	0.63	0.78	2	1	0.6	1.6

uration. The DQQ configuration permits the minimization of the background at the focal plane. This is done by the removal of the primary beam directly after the target, such that only the transmitted ions are further focused on the detectors. An additional dipole is sometimes used for an improved rejection. As compared to other separators, the gas-filled VAMOS has a large angular acceptance. Together with the high transport efficiency and detector size, it leads to the unprecedented transmission values discussed in section 3.2.

The absence of focusing behind the dipole at VAMOS is less critical due to the large size of the detectors at the focal plane [17]. For the current configuration, the maximum magnetic rigidity  $B\rho_{max}$  is lower than that available elsewhere. The use of an alternative configuration permits increasing  $B\rho_{max}$  up to 2.2 T-m while keeping a reasonably good angular acceptance ( $\Omega \sim 45$  msr). The large dispersion and large area of the focal plane detectors leads to a selective and efficient measurement of the evaporation residues.

Figure 12 shows a comparison of the transmission at VAMOS, at the velocity filter SHIP [28] and at the gas-filled separator RITU [13]. The transmission of representative neutron evaporation channels produced in various reactions is displayed as a function of the reaction asymmetry  $A_p/A_t$ . The values predicted at VAMOS are much larger than those obtained at existing devices.

#### 4. Future developments

The gas-filled mode of VAMOS was implemented without any major modification of the existing setup. Hence, modifications of the setup are necessary for further optimiz-

ing the capabilities of VAMOS in this mode. Due to mechanical constraints related to the H-core shaped geometry of the dipole magnet, the beam dump was located inside the dipole chamber (Fig. 1). Changing the position of the beam dump beyond the dipole, with additional shielding (Fig. 13), is expected to prevent particles scattered from the beam dump to reach the detectors. As mentioned earlier, a carbon foil was used in the present measurement to isolate the vacuum of the beam line from the gas-filled region. The use of a differential pumping improves the properties of the beam at the target position. Both these changes would allow the use of higher beam intensities. A rotating target is already available to accept these high beam intensities. The isotopic identification of the ER can be made correlating in position and time the ER and its decay [40]. The use of the large size and highly-segmented Si wall MUSETT (4 DSSSD elements of 10 cm  $\times$  10 cm area with 128  $\times$  128 elements each) is envisaged for this purpose [41].

#### 5. Conclusions

A new gas-filled operation mode was implemented at the VAMOS spectrometer at GANIL. It is shown to be a highly selective and efficient  $0^\circ$  spectrometer for the evaporation residues produced in fusion reactions. For the  $^{40}\text{Ca}+^{150}\text{Sm}$  system at 196 MeV, a rejection factor better than  $10^{10}$  was achieved for the direct beam. The transmission efficiency of the evaporation residues was estimated between 80% and 95%, depending on the evaporation channel. The planned modifications are expected to further improve the sensitivity of the setup. To fully exploit the potential of

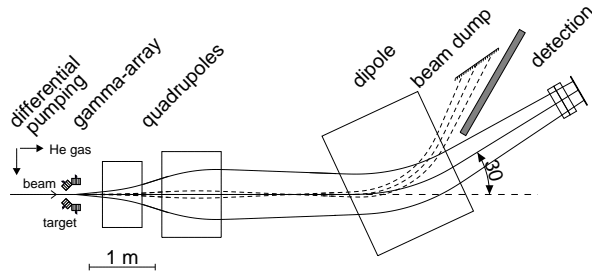


Fig. 13. Schematic layout of the planned upgrade of the gas-filled VAMOS.

next-generation facilities based on intense radioactive heavy-ion beams such as SPIRAL2, a very high rejection of the beam is required for fusion reactions in symmetric and inverse kinematics. The new gas-filled mode extends the capabilities of the large-acceptance VAMOS when operated at  $0^\circ$ , opening new avenues for the study of nuclear structure and reaction dynamics at the limits. The successful operation of the gas filled mode adds to the versatility of the already existing vacuum mode of VAMOS.

## 6. Acknowledgments

We would like to thank J. Ropert for his technical contribution to the experimental set-up as well as the GANIL accelerator staff for smooth operation and high beam quality. We are also thankful to the GSI target laboratory and G. Fremont for making the  $^{150}\text{Sm}$  targets. S. Pullanhiotan is acknowledged for his critical reading of the manuscript. M. Mazzocco and J. Saren are thanked for providing the transmission data of SHIP and RITU, respectively, and for fruitful discussion. We would like to thank A. Spitaels for help during data taking.

## References

[1] R. Anne *et al.*, Nucl. Instr. and Meth. **B** 70 (1992) 276.  
 [2] G. Munzenberg *et al.*, Nucl. Instr. and Meth. 186 (1981) 423.  
 [3] C.N. Davids, Nucl. Instr. and Meth. **B** 204 (2003) 124.  
 [4] M. Leino, Nucl. Instr. and Meth. **B** 204 (2003) 129.  
 [5] A. Ghiorso *et al.*, Nucl. Instr. and Meth. **A** 269 (1988) 192.  
 [6] B. Cohen and C. Fulmer, Nucl. Phys. 6 (1968) 547.  
 [7] M. Paul *et al.*, Nucl. Instr. and Meth. **A** 277 (1988) 418.

[8] J.F.C. Cocks *et al.*, Eur. Phys. J. **A** 3 (1998) 17.  
 [9] K. Sistemich *et al.*, Nucl. Instr. and Meth. 130 (1975) 491.  
 [10] T.M. Cormier *et al.*, Nucl. Instr. and Meth. 212 (1983) 185.  
 [11] V. Ninov *et al.*, Nucl. Instr. and Meth. **A** 357 (1995) 486.  
 [12] S. Nath *et al.*, Nucl. Instr. and Meth. **A** 576 (2007) 403.  
 [13] J. Saren *et al.*, Contribution to the TASC09 workshop, Darmstadt, Germany.  
 [14] A.M. Stefanini *et al.*, Nucl. Phys. **A** 701 (2002) 217.  
 [15] A. Cunsolo *et al.*, Nucl. Instr. and Meth. **A** 484 (2002) 56.  
 [16] H. Savajols for the VAMOS collaboration, Nucl. Instr. and Meth. **B** 204 (2003) 146.  
 [17] S. Pullanhiotan *et al.*, Nucl. Instr. and Meth. **A** 593 (2008) 343.  
 [18] S. Bhattacharyya *et al.*, Phys. Rev. Lett. 101 (2008) 032501.  
 [19] A. Shrivastava *et al.*, Phys. Rev. **C** 80 (2009) 051305(R).  
 [20] A. Obertelli *et al.*, Phys. Lett. **B** 633 (2006) 33.  
 [21] J. Simpson *et al.*, Heavy Ion Phys. 11 (2000) 159.  
 [22] F. Méot *et al.*, Nucl. Instr. and Meth. **A** 427 (1999) 353.  
 [23] J.F. Ziegler, SRIM - The Stopping Range of Ions in Matter, <http://www.srim.org/index.htm>.  
 [24] J.B. Moulton *et al.*, Nucl. Instr. and Meth. 157 (1978) 325.  
 [25] A. Gavron *et al.*, Phys. Rev. **C** 20 (1980) 230.  
 [26] K. Subotic *et al.*, Nucl. Instr. and Meth. **A** 481 (2002) 71.  
 [27] Ch. Theisen *et al.*, unpublished.  
 [28] M. Mazzocco *et al.*, Nucl. Instr. and Meth. **B** 266 (2008) 3467.  
 [29] M. Dahlinger *et al.*, Nucl. Instr. and Meth. 219 (1984) 513.  
 [30] A. Semchenkov, Nucl. Instr. and Meth. **B** 266 (2008) 4153.  
 [31] D. Montanari *et al.*, submitted to Nucl. Instr. and Meth. **A**.  
 [32] J. Pakarinen *et al.*, Phys. Rev. **C** 72 (2005) 011304(R).  
 [33] K.E. Gregorich *et al.*, Phys. Rev. **C** 72 (2005) 014605.  
 [34] D. Bazzacco *et al.*, Nucl. Phys. **A** 746 (2004) 248c.  
 [35] J.J. Ressler *et al.*, Nucl. Instr. and Meth. **B** 204 (2003) 141.  
 [36] Yu.A. Lazarev *et al.*, Proceedings of the International School-Seminar on Heavy Ion Physics, Dubna, Russia, 1993, Vol. 2, p. 497.  
 [37] K. Morita *et al.*, Nucl. Instr. and Meth. **B** 70 (1992) 220.  
 [38] V. Ninov *et al.*, Proceedings of the ENAM98, Bellaire, Michigan, 1998, AIP Conf. Proc. 455 (1998) 704.  
 [39] M. Leino, Nucl. Instr. and Meth. **B** 99 (1995) 653.  
 [40] R.S. Simon *et al.*, Z. fur Phys. **A** 325 (1986) 197.  
 [41] Ch. Theisen *et al.*, to be published.